Dalton Transactions

Synthesis of a Monocationic μ–Nitrido-Bridged Iron Porphycene Dimer and Its Methane Oxidation Activity

Journal:	*Dalton Transactions*
Manuscript ID	DT-ART-08-2021-002922.R1
Article Type:	Paper
Date Submitted by the Author:	08-Oct-2021
Complete List of Authors:	Yamada, Yasuyuki; Nagoya University, Research Center for Materials Science Miwa, Yusuke; Nagoya University, Department of Chemistry Toyoda, Yuka; Nagoya University, Department of Chemistry Yamaguchi, Tomoo; Nagoya University, Department of Chemistry Akine, Shigehisa; Kanazawa University, Graduate School of Natural Science and Technology Tanaka, Kentaro; Nagoya University, Department of Chemistry, Graduate School of Science

PAPER

Synthesis of a Monocationic μ–Nitrido-Bridged Iron Porphycene Dimer and Its Methane Oxidation Activity

Received 00th January 20xx,
Accepted 00th January 20xx

DOI: 10.1039/x0xx00000x

Yasuyuki Yamada,*[a,b,c] Yusuke Miwa,[a] Yuka Toyoda,[b] Tomoo Yamaguchi,[a] Shigehisa Akine[d] and Kentaro Tanaka *[a]

Herein, we report on the synthesis of a monocationic μ-nitrido-bridged iron porphycene dimer, a structural analog of a monocationic μ-nitrido-bridged iron phthalocyanine dimer, which is known to be one of the most potent molecule-based catalysts for CH_4 oxidation. ^{1}H-NMR and single-crystal X-ray structural analyses showed that the porphycene complex includes two Fe(IV) ions, and the structure around the Fe-N=Fe core is quite similar to that of the monocationic μ-nitrido-bridged iron phthalocyanine dimer. Although CH_4 was oxidized into MeOH, HCHO, and HCOOH in the presence of a silica-supported catalyst of this monocationic μ-nitrido-bridged iron porphycene dimer in an acidic aqueous solution containing excess H_2O_2, its reactive intermediate was not a high-valent iron-oxo species, as in the case of a monocationic μ-nitrido-bridged iron phthalocyanine dimer, but •OH. It is suggested that the high-valent iron-oxo species of the μ-nitrido-bridged iron porphycene dimer is gradually decomposed under these reaction conditions, and the decomposed compound catalyzes a Fenton-type reaction. This result indicates that the stability of the oxo-species is indispensable for achieving high catalytic methane oxidation activity using a μ-nitrido-bridged iron porphyrinoid dimer with a Fe-N=Fe core as a catalyst.

Introduction

μ-Nitrido-bridged iron porphyrinoid dimers, in which one nitrogen atom bridges the iron centers of two iron porphyrinoids, are a unique class of metallo-porphyrinoids. The first example of this structure was a μ-nitrido-bridged FeTPP dimer (TPP = 5,10,15,20-tetraphenylporphyrin) reported by Cohen et al.[1] Inspired by this study, Ercholani et al. synthesized a μ-nitrido-bridged FePc dimer (Pc = phthalocyanine).[2] After these reports, several groups extensively investigated the structure of these complexes to clarify that neutral complexes of μ-nitrido-bridged iron porphyrinoid dimers possess one Fe(III) and one Fe(IV) ion, whereas 1e$^-$-oxidized monocationic complexes include two Fe(IV) ions. Because these complexes are quite stable in air, their unique physical properties have also been investigated, using various techniques including EPR, absorption, Mössbauer, XANES, EXAFS spectroscopy, and electrochemical measurements.[3-12]

Recently, increasing attention has been focused on the application of these μ-nitrido-bridged iron porphyrinoid dimers as oxidation catalysts for light alkanes including methane.[13-21] Methane is expected to be a next-generation chemical feedstock because it is abundant in nature as natural gas or methane hydrate. However, since methane has high chemical stability and possesses a particularly high C-H bond dissociation energy among a large variety

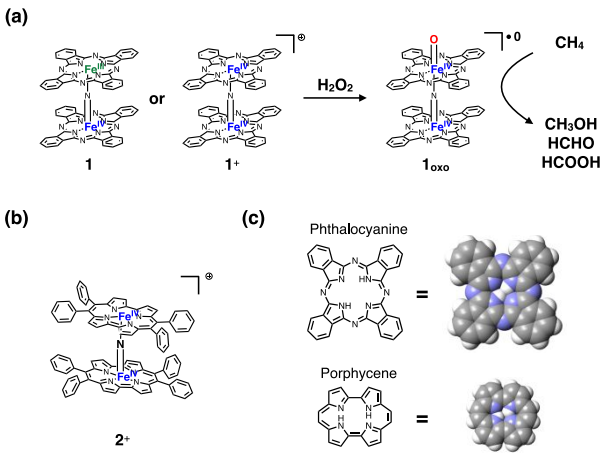

Figure 1 (a) Formation of high-valent iron oxo species $\mathbf{1_{oxo}}$ showing a potent CH_4 oxidation activity, from **1** or $\mathbf{1^+}$ through the reaction with H_2O_2. (refs. 14, 15 and 21) (b) A monocationic μ-nitrido-bridged iron porphycene dimer synthesized in this work ($\mathbf{2^+}$). (c) Comparison of the structures of a phthalocyanine and a porphycene. Both of the chemical structures and CPK models are shown.

[a] Department of Chemistry, Graduate School of Science, Nagoya University, Furo-cho, Chikusa-ku, Nagoya 464-8602, Japan.
[b] Research Center for Materials Science, Nagoya University, Furo-cho, Chikusa-ku, Nagoya 464-8602, Japan.
[c] JST, PRESTO, 4-1-8 Honcho, Kawaguchi, Saitama, 332-0012, Japan.
[d] Graduate School of Natural Science and Technology, Kanazawa University, Kakuma-machi, Kanazawa 920-1192, Japan
†E-mail: yy@chem.nagoya-u.ac.jp, kentaro@chem.nagoya-u.ac.jp
Electronic Supplementary Information (ESI) available: [details of any supplementary information available should be included here]. See DOI: 10.1039/x0xx00000x

of organic compounds (104.9 kcal/mol), direct and low-temperature C-H bond activation of methane has been recognized as a difficult challenge in the field of catalytic chemistry.[22,23] Sorokin et al. demonstrated that a μ-nitrido-bridged iron phthalocyanine dimer **1** showed high catalytic methane oxidation activity in an acidic aqueous solution containing excess H_2O_2 (Figure 1a).[15] The reactive intermediate was the high-valent iron-oxo species, $\mathbf{1}_{oxo}$, generated *in situ*.[16] It was confirmed that the 1e⁻-oxidized monocationic species of **1** (**1**⁺) also showed similar methane oxidation activity through the same high-valent iron oxo species.[21] Since these are some of the few molecule-based artificial methane oxidation catalysts reported to date, much effort has been paid to understand the correlation between their electronic structure and reactivity.[13,14,20,24,25] Theoretical calculations based on these data have revealed that the μ-nitrido-bridged dinuclear iron structure plays a dominant role in methane oxidation activity.[26–28] For example, de Visser et al. calculated that the origin of the high reactivity of the iron oxo species is related to the orbital mixing pattern along the Fe=N-Fe=O axis, where the axial FePc=N- moiety donates sufficient electron density to FePc=O to affect not only the strength of the O-H bond of the iron hydroxo complex formed during methane oxidation, but also the basicity of the terminal oxygen.[26]

It was reported that a μ-nitrido-bridged iron porphyrin dimer also shows potent oxidation activity, similar to the μ-nitrido-bridged iron phthalocyanine dimer.[16] Moreover, we previously demonstrated that a μ-nitrido-bridged heterodimer of an iron porphyrin and an iron phthalocyanine constructed in a supramolecular assembly acts as a potent methane oxidation catalyst.[18] Based on these results, it can be assumed that μ-nitrido-bridged iron porphyrinoid dimers with a Fe-N=Fe core generally show high catalytic methane oxidation activity. Since the catalytic activity of μ-nitrido-bridged iron phthalocyanine dimers is largely affected by differences in the electronic structure of the phthalocyanine cores,[17,20,21] it would be interesting to know if higher methane oxidation activity can be achieved by using other types of porphyrinoids such as corroles and corphycenes as the core of a μ-nitrido-bridged iron porphyrinoid dimer. However, there are no reports on the synthesis of μ-nitrido-bridged dimers using iron porphyrinoids other than iron porphyrin and iron phthalocyanine, although many different kinds of porphyrinoids have been synthesized to date.

In this study, we report on the first synthesis of a monocationic μ–nitrido-bridged iron porphycene dimer (**2**⁺, Figure 1b) and its methane oxidation activity. Porphycene is an important class of porphyrinoids and has a rectangular-shaped narrow cavity compared to porphyrins and phthalocyanines (Figure 1c), which renders the coordination structures and reactivity of the metal complexes different from those of porphyrins and phthalocyanines.[29,30] Therefore, we became interested in the structure, physical properties, and catalytic methane oxidation activity of **2**⁺.

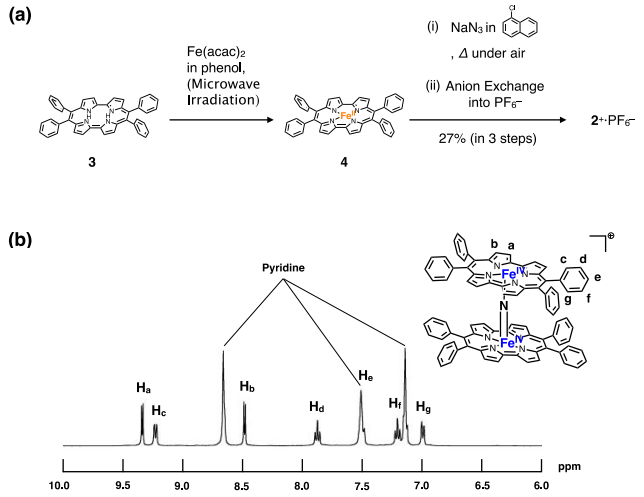

Figure 2 (a) Synthesis of **2**⁺·PF_6^-. (b) ^{1}H-NMR spectrum of **2**⁺·PF_6^- in pyridine-d_5.

Results and Discussion

The synthetic route to **2**⁺·PF_6^- is summarized in Figure 2a. A porphycene **3** was chosen as the starting material. Recently, Ono and Hisaeda et al. developed an efficient synthesis of **3** from 5,6-diphenyl dipyrroethane (up to 65%), although porphycene syntheses generally suffer from relatively low yield.[31] After **3** was converted into its iron complex **4**, **4** was heated with NaN_3 in 1-chloronaphthalene in the air. During this procedure, a neutral μ-nitrido-bridged iron porphycene dimer (**2**) was first generated and was presumably oxidized by air to form its 1e⁻-oxidized monocationic form (**2**⁺). Finally, the counter anion was exchanged with PF_6^- to give the desired **2**⁺·PF_6^- product. **2**⁺·PF_6^- has good solubility in many organic solvents such as acetone, CH_3CN, CH_2Cl_2, and $CHCl_3$, presumably because the peripheral phenyl groups inhibit the formation of stacked aggregates.

^{1}H-NMR, MALDI-TOF MS, and elemental analysis were performed to characterize **2**⁺·PF_6^-. In the MALDI-TOF MS spectrum shown in Figure S1 in the Supporting Information, the signal corresponding to that of **2**⁺·PF_6^- was observed at *m/z* = 1351, which is consistent with the theoretical isotope pattern. It has been reported that a neutral μ-nitrido-bridged FeTPP dimer containing Fe(III) and Fe(IV) showed significant broadening of the ^{1}H NMR signals, while its monocationic species containing two Fe(IV) centers showed sharp ^{1}H NMR signals because the two Fe(IV) centers interacted with each other in an antiferromagnetic fashion.[3,4,10] The fact that **2**⁺·PF_6^- shows sharp ^{1}H NMR signals as shown in Figure 2b suggests that the two Fe centers in **2**⁺·PF_6^- are both in the Fe(IV) state and interact antiferromagnetically *via* a nitrogen bridge. Another characteristic feature of the ^{1}H-NMR spectrum of **2**⁺·PF_6^- is that two sets of signals corresponding to those of *the o*- and *m*-protons of the peripheral phenyl groups are observed, indicating that the rotation of the peripheral phenyl groups is restricted due to steric repulsion between the phenyl groups and the porphycene rings.

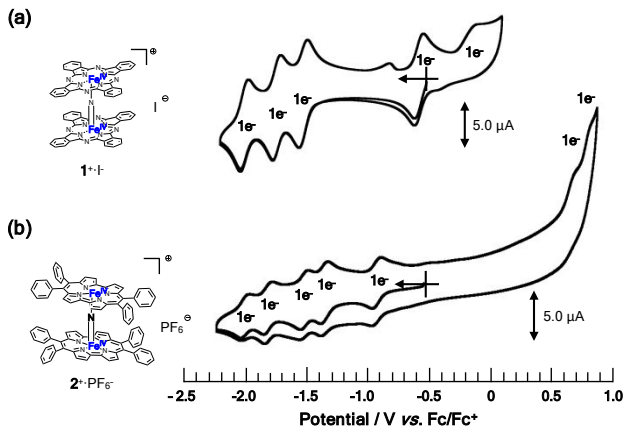

Figure 3 Cyclic voltammograms of (a) $\mathbf{1}^{+}\cdot I^{-}$ and (b) $\mathbf{2}^{+}\cdot PF_6^{-}$ in a pyridine solution containing 100 mM of $^{n}Bu_4N^{+}\cdot PF_6^{-}$ at room temperature. [Substrate] = 200 μM, [Scan rate] = 100 mV/s.

A cyclic voltammogram of $\mathbf{2}^{+}\cdot PF_6^{-}$ was measured in a pyridine solution (200 μM) containing 100 mM $^{n}Bu_4N^{+}\cdot PF_6^{-}$ and compared with that of $\mathbf{1}^{+}\cdot I^{-}$, as shown in Figure 3. We used pyridine as a solvent because pyridine is a good solvent for $\mathbf{1}^{+}\cdot I^{-}$. As for the voltammogram of a monomeric porphycene, M. Gross et al. investigated the detailed redox properties of a 2,7,12,17-tetra-*n*-propylporphycene iron (III) chloride (ClFeTprPpc).[32] Based on their electrochemical and spectroelectrochemical measurements, they concluded that the first and second reduction waves can be attributed to those of Fe(III)/Fe(II) and TPrPpc/TPrPpc$^{\bullet-}$, respectively, whereas the first oxidation wave is attributed to that of TPrPpc$^{\bullet+}$/TPrPpc. Considering that $\mathbf{2}^{+}\cdot PF_6^{-}$ has two Fe(IV) centers, which have even higher redox states than the iron ions in ClFeTrPpc, the 1st (–0.90 V vs. Fc^{+}/Fc), 2nd (–1.32 V), 3rd (–1.49 V), and 4th (–1.78 V) reduction waves are assignable to those of Fe(IV)Fe(IV)/Fe(III)Fe(IV), Fe(III)Fe(IV)/Fe(III)Fe(III), Fe(III)Fe(III)/Fe(II)Fe(III), and Fe(II)Fe(III)/Fe(II)Fe(II), respectively. In the case of the monocationic μ-nitrido-bridged iron phthalocyanine dimer $\mathbf{1}^{+}\cdot I^{-}$, the 1st (–0.58 V vs. Fc^{+}/Fc), 2nd (–1.52 V), 3rd (–1.74 V), and 4th (–2.00 V) reduction waves are assigned to the reductions of the iron centers. Given that the reduction of the porphycene ring in the redox process of ClFeTrPpc occurs at a more negative potential than the reduction of the Fe(II) center,[32] it is assumed that the 5th reduction of $\mathbf{2}^{+}\cdot PF_6^{-}$ at –1.98 V might be the redox reaction of the porphycene center. On the other hand, the 1st (0.68 V) and 2nd (0.79 V) oxidation waves of $\mathbf{2}^{+}\cdot PF_6^{-}$ are assignable to those of the 1e^{-}-oxidation of the porphycene center, based on the redox properties of ClFeTrPpc. The difference in the redox character of $\mathbf{2}^{+}\cdot PF_6^{-}$ from that of $\mathbf{1}^{+}\cdot I^{-}$ is that the 1st reduction of $\mathbf{2}^{+}\cdot PF_6^{-}$, corresponding to that of Fe(IV)Fe(IV)/Fe(III)Fe(IV) appears to have a more negative potential ($\Delta E^{\circ\prime}$ = 0.32 V) than that of $\mathbf{1}^{+}\cdot I^{-}$, whereas the other redox waves including the 2nd, 3rd, and 4th reductions and the 1st and 2nd oxidations appear at more positive potentials.

A comparison of the UV-Vis spectra of $\mathbf{1}^{+}\cdot I^{-}$ and $\mathbf{2}^{+}\cdot PF_6^{-}$ in pyridine is shown in Figure 4. $\mathbf{1}^{+}\cdot I^{-}$ shows intense absorptions corresponding to the Q-band of phthalocyanine at 500–750 nm. Although $\mathbf{2}^{+}\cdot PF_6^{-}$ also shows peaks corresponding to the Q-band of porphycene between 500 and 750 nm, the absorption coefficients

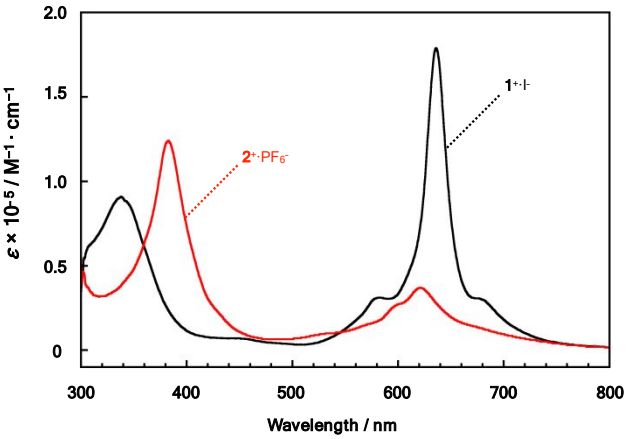

Figure 4 UV-Vis spectra of $\mathbf{1}^{+}\cdot I^{-}$ (black curve) and $\mathbf{2}^{+}\cdot PF_6^{-}$ (red curve) in pyridine at 20 °C.

(ε) of these peaks are much smaller than those of $\mathbf{1}^{+}\cdot I^{-}$. The peak for $\mathbf{2}^{+}\cdot PF_6^{-}$ at 383 nm is assignable to that of the Soret band, which appears at a much higher wavelength than that of $\mathbf{1}^{+}\cdot I^{-}$. A similar tendency in the difference between the Soret and Q-bands was observed in comparing the UV-Vis spectra of the metal-free monomeric porphycene and phthalocyanine, as shown in Figure S2 in the Supporting Information. These differences in the voltammograms and UV spectra are apparently due to the difference in the structure of the porphyrinoids.

A comparison of the single-crystal structure of $\mathbf{2}^{+}\cdot PF_6^{-}$ with that

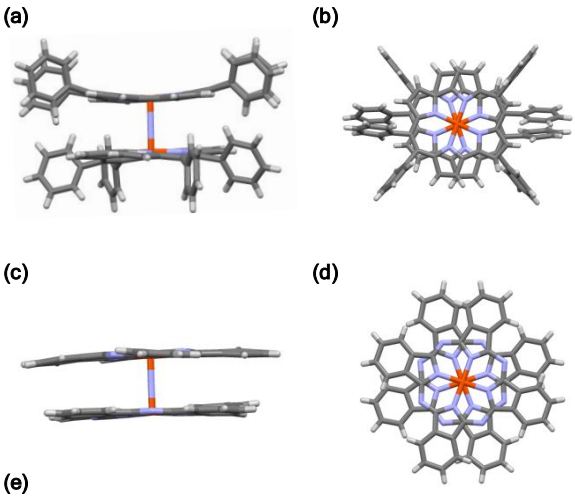

(e)

	$\mathbf{2}^{+}\cdot PF_6^{-}$	$\mathbf{1}^{+}\cdot I^{-}$
Fe- N(porphyrinoid)	1.93 Å	1.93 Å
Fe- N(μ)	1.64 Å	1.64(2) Å
N(μ)- Fe- N(porphyrinoid)	92.5(2)º	92.3(2)º

Figure 5 (a) Side and (b) top views of the single crystal X-ray structure of $\mathbf{2}^{+}\cdot PF_6^{-}$. PF_6^{-} and coordinating pyridines were omitted for clarity. (c) Side and (d) top views of the single crystal X-ray structure of $\mathbf{1}^{+}\cdot I^{-}$ (ref. 33). I^{-} and coordinating pyridines, crystalline solvents were omitted for clarity. (e) Comparison of some mean bond lengths and angles of $\mathbf{2}^{+}\cdot PF_6^{-}$ and $\mathbf{1}^{+}\cdot I^{-}$.

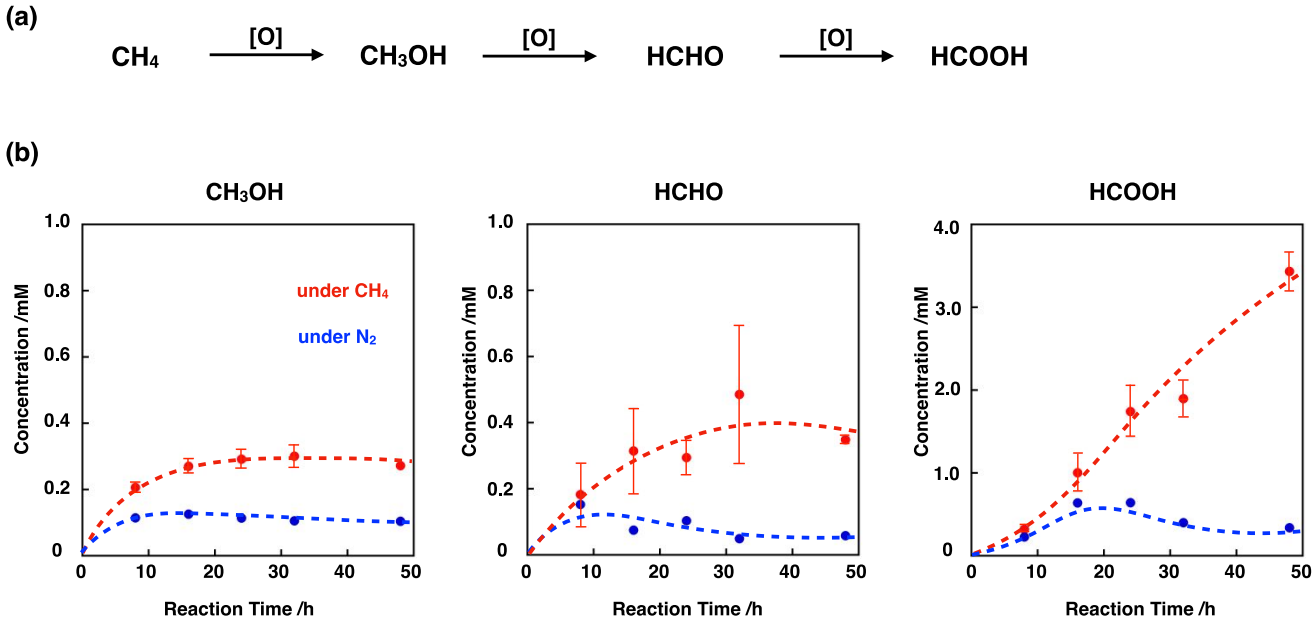

Figure 6 (a) Stepwise methane oxidation reaction. (b) Time dependence of concentrations of each oxidized product (MeOH, HCHO, and HCOOH) observed in the reaction under methane atmosphere of 1.0 MPa (red closed circle) or in the absence of methane (under 1.0 MPa of N_2, blue closed circle) in an aqueous solution (3.0 mL) containing **2**$^{+}$·PF_6^-/SiO_2 (55 μM as **2**$^{+}$·PF_6^-), H_2O_2 (189 mM), and TFA (51 mM) at 60 °C. Error bars indicate standard deviations of three independent methane oxidation reactions.

of **1**$^{+}$·I^-[33] is shown in Figure 5. The ORTEP representation of the molecular structure of **2**$^{+}$·PF_6^- is shown in Figure S3. As can be seen from the top view (Figure 5b), the upper and lower porphycene rings of **2**$^{+}$ are twisted by 47°. Considering that the upper and lower phthalocyanine rings of **1**$^{+}$ are also twisted by 45° (Figure 5d), this is not only due to steric repulsion between the peripheral phenyl groups of the porphycene ring of **2**$^{+}$ but also to repulsion between the two porphycene rings. As confirmed by the ^{1}H NMR spectra, it is obvious that the rotation of the peripheral phenyl groups of is **2**$^{+}$ significantly suppressed by steric repulsion between the phenyl groups and that between the phenyl groups and the porphycene rings. On the other hand, the two phthalocyanine rings are almost flat in **1**$^{+}$·I^-, whereas the two rings are slightly distorted in **2**$^{+}$·PF_6^- because of steric repulsion between the peripheral phenyl groups and the porphycene cores.

The mean bond distance between the four porphycene nitrogens and the coordinated iron(IV) ions in **2**$^{+}$·PF_6^- is 1.93 Å, which is consistent with that of **1**$^{+}$·I^- (1.93 Å), as summarized in the table shown in Figure 5e. The average bond angle of the μ-nitrogen–Fe–nitrogen(porphyrinoid) of **2**$^{+}$·PF_6^- is 92.5°, which is almost identical to that of **1**$^{+}$·I^-. The mean distances between the μ-nitrogen and the two iron ions are 1.64 Å for **2**$^{+}$·PF_6^- and 1.64(2) Å for **1**$^{+}$·I^-. Overall, the structure around the Fe-N-Fe axis in **2**$^{+}$·PF_6^- is quite similar to that of **1**$^{+}$·I^-.

A silica-supported catalyst of **2**$^{+}$·PF_6^- (**2**$^{+}$·PF_6^-/SiO_2) was prepared to investigate the methane oxidation activity because **2**$^{+}$·PF_6^- is not soluble in an aqueous solution. Heterogeneous methane oxidation using **2**$^{+}$·PF_6^-/SiO_2 was carried out at 60 °C in an aqueous solution containing excess H_2O_2 (189 mM) and TFA (51 mM) under a methane atmosphere of 1.0 MPa. The amounts of oxidation products (methanol, formaldehyde, and formic acid) were determined by GC-MS analysis. As shown in Figure 6b and Table S1 and S2 in the Supporting Information, methanol, formaldehyde, and formic acid were detected during the oxidation process. However, the color of the porphycene gradually faded during the reaction and almost disappeared after 48 h, indicating that the catalyst gradually decomposes under these reaction conditions.

We calculated the effective total turnover (TTN_{eff}) defined by the following equations (i) and (ii) to confirm whether the methane oxidation reaction by **2**$^{+}$·PF_6^- actually proceeded. TTN is based on the idea that methane is oxidized in a stepwise manner, as shown in Figure 6a. The oxidized products observed in the absence of methane (under N_2 atmosphere) were presumably derived from the decomposed catalyst and also from organic solvent adsorbed on the silica surface during the preparation of **2**$^{+}$·PF_6^-/SiO_2.[18-21] Actually, the color of **2**$^{+}$·PF_6^- was gradually faded in the absence of methane. Therefore, it is considered that TTN_{eff} should indicate the actual amount of the oxidized methane in this reaction condition.

$$TTN_{eff} = TTN_{(CH4)} - TTN_{(N2)} \quad \text{(i)}$$

$$TTN_{(CH4)} \text{ or } TTN_{(N2)} = (C_{MeOH} + 2 \times C_{HCHO} + 3 \times C_{HCOOH}) / C_{Cat} \quad \text{(ii)}$$

As shown in Figure 7a, TTN_{eff} was almost negligible at the initial stage of the oxidation; however, it started to increase after 8 h. The increase in TTN_{eff} indicates that methane was oxidized under these reaction conditions. Considering that **2**$^{+}$·PF_6^-/SiO_2 gradually faded in color during the reaction, this suggests that the decomposed product of **2**$^{+}$·PF_6^- shows methane oxidation activity.

To confirm the possibility of a Fenton-type reaction, in which the hydroxyl radical (•OH) acts as a reactive species instead of high-valent iron oxo species, the oxidation reaction was carried out in the presence of an excess of the radical scavenger Na_2SO_3.[34] It was demonstrated that TTN_{eff} was significantly decreased under this condition, as shown in entry 6 of Table S1. This is in contrast to the fact that the methane oxidation was hardly quenched by Na_2SO_3 in the reaction using μ-nitrido-bridged iron phthalocyanine dimer as a

catalyst under the same reaction conditions,[21] where the high-valent iron-oxo species acted as a reactive intermediate. These results suggest that the reactive intermediate in the reaction using $\mathbf{2}^{+}\cdot PF_6^{-}/SiO_2$ is •OH generated from H_2O_2. It is assumed that the decomposed $\mathbf{2}^{+}\cdot PF_6^{-}$ might act as a catalyst for the generation of •OH. It should also be noted that color-fading of the catalyst was also observed even in the presence of excess Na_2SO_3, implying that the fading is not due to •OH. This suggests that the reactive iron-oxo species of $\mathbf{2}^{+}\cdot PF_6^{-}$ generated through the reaction with H_2O_2 could be so unstable that it decomposes immediately under these reaction conditions. Taking these results into consideration, the reaction mechanism of methane oxidation by $\mathbf{2}^{+}\cdot PF_6^{-}$ can be summarized as shown in Figure 7b.

Conclusions

In this study, we reported on the synthesis of the first example of a μ-nitrido-bridged iron porphycene dimer $\mathbf{2}^{+}\cdot PF_6^{-}$. ^{1}H NMR analysis indicated that $\mathbf{2}^{+}\cdot PF_6^{-}$ includes two Fe(IV) centers, as in the case of a monocationic μ-nitrido-bridged iron phthalocyanine dimer $\mathbf{1}^{+}\cdot I^{-}$. Single crystal X-ray structural analysis demonstrated that the structure around the Fe-N-Fe center of $\mathbf{2}^{+}\cdot PF_6^{-}$ was quite similar to that of $\mathbf{1}^{+}\cdot I^{-}$. Electrochemical measurements showed that $\mathbf{2}^{+}\cdot PF_6^{-}$ shows five reversible reduction waves and two irreversible oxidation waves in the potential range between –2.2 to +0.8 V vs. Fc^{+}/Fc.

We investigated the methane oxidation reaction using a silica-supported catalyst $\mathbf{2}^{+}\cdot PF_6^{-}/SiO_2$ in an acidic aqueous solution containing excess H_2O_2 at 60 °C since $\mathbf{1}^{+}\cdot I^{-}/SiO_2$ showed catalytic methane oxidation activity under the same reaction conditions. Although methane was actually oxidized into methanol, formaldehyde, and formic acid, it was also found that $\mathbf{2}^{+}\cdot PF_6^{-}$ gradually decomposed under the reaction conditions. In the case of methane oxidation by $\mathbf{1}^{+}\cdot I^{-}$, the reactive intermediate was the high-valent iron-oxo species generated from the reaction with H_2O_2. However, our experiments suggested that the high-valent iron oxo species of $\mathbf{2}^{+}\cdot PF_6^{-}$ is unstable and prone to decomposition under these reaction conditions. The decomposed product acts as a catalyst for the generation of •OH from H_2O_2 to proceed with the methane oxidation reaction. It is interesting that $\mathbf{2}^{+}\cdot PF_6^{-}$, with a Fe-N-Fe structure similar to that in $\mathbf{1}^{+}\cdot I^{-}$, did not show high methane oxidation activity due to instability of the high-valent iron oxo species. Apparently, the structural difference between porphycene and phthalocyanine is reflected in a difference in the stability of the high-valent iron oxo species. This suggests that controlling the high stability of the high-valent iron oxo species is also an important factor in achieving high catalytic methane oxidation activity by using a catalyst with a μ-nitrido-bridged iron porphyrinoid dimer core. In order to achieve high stability of the iron-oxo species based on the μ-nitrido-bridged iron porphycene core, the introduction of appropriate peripheral substituents onto the porphycene ring might be an effective approach.

Experimental

General All reagents and solvents were purchased at the highest commercial quality available and used without further purification, unless otherwise stated. A metal-free porphycene **3** was synthesized according to the reported procedure.[31] ^{1}H NMR spectra were recorded on a JEOL JNM-ECS400-A (400 MHz for ^{1}H) spectrometer at a constant temperature of 298 K. Elemental analysis was performed on a Yanaco MT-6 analyzer. The absorption spectrum was recorded with a Hitachi U-4100 spectrophotometer in pyridine solutions at 20 ± 0.1 °C in 1.0 cm quartz cells. MALDI-TOF MS was performed on Bruker Daltonics ultraXtreme using α-CHCA as a matrix.

Synthesis of $\mathbf{2}^{+}\cdot PF_6^{-}$. A metal-free porphycene **3** (151 mg, 0.25 mmol) and $Fe(acac)_2$ (433 mg, 1.70 mmol) in phenol (45 mL) was heated at 190 °C for 3 h under microwave irradiation. After cooling to room temperature, the reaction mixture was dissolved in CH_2Cl_2. The undissolved solid was removed by filtration. The filtrate was concentrated under reduced pressure. The residual solid was washed with H_2O (100 mL × 3) to give an iron porphycene **4** as a green solid (242 mg). This was used for the next reaction without further purification. MALDI-TOF MS: *m/z* = 668.31 : calcd for $C_{44}H_{28}FeN_4$ ($[M]^+$) found: 668.17.

A mixture of **4** (100 mg, 0.15 mmol), NaN_3 (98.5 mg, 1.51 mmol) and 1-chloronaphtalene (2.5 mL) was heated under air at 280 °C for 2 h. After cooling to room temperature, the reaction mixture was diluted with CH_2Cl_2 (200 mL). The solution was washed H_2O (100 mL × 3), and then, evaporated to give bluish green crude solid. The crude was purified by silica gel column chromatography (5 cmϕ × 11

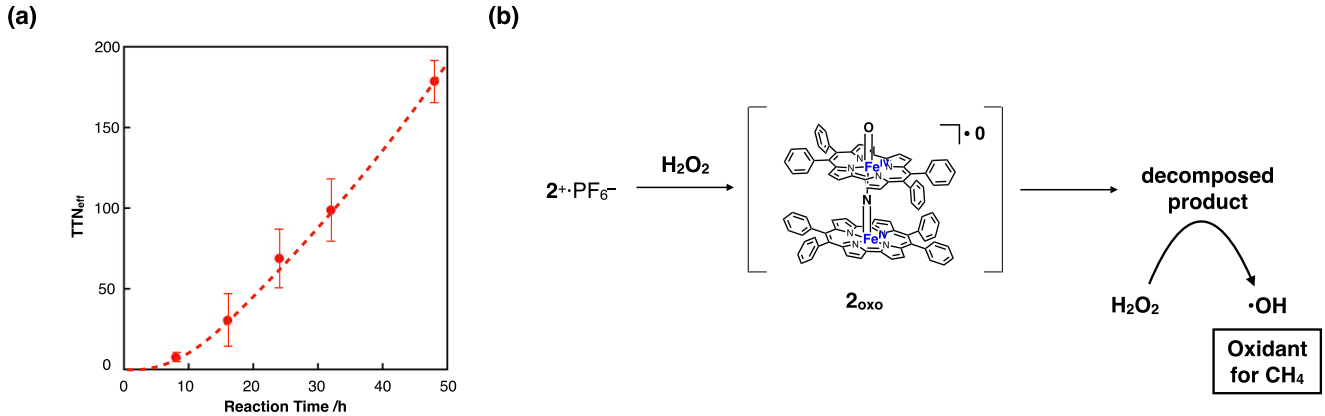

Figure 7 (a) Time dependence of TTN_{eff} for methane oxidation by $\mathbf{2}^{+}\cdot PF_6^{-}/SiO_2$. (b) Proposed mechanism of methane oxidation using $\mathbf{2}^{+}\cdot PF_6^{-}/SiO_2$ in an acidic aqueous solution containing H_2O_2.

cm , CH_2Cl_2:MeOH = 40:1 – 20:1) to yield bluish green solid (30 mg). After the solid was dissolved in CH_3CN (15 mL), KPF_6 (419 mg, 2.28 mmol) was added to the solution. Addition of H_2O (15 mL) gave blue precipitate, which was collected by centrifugation and washed with H_2O to give the title compound as a bluish green solid (19 mg, 27% (from **3**)). ^{1}H-NMR (400 MHz, pyridine-d_5/TMS) : δ = 9.42 (d, J = 4.9 Hz, 8H), 9.30 (d, J = 7.6 Hz, 8H), 8.56 (d, J = 4.9, 8H), 7.94 (t, J = 7.4 Hz, 8H), 7.58 (m, 8H), 7.27 (t, J = 7.4 Hz, 8H), 7.06 (d, J = 7.4 Hz, 8H). MALDI-TOF MS: m/z = 1351.34 : calcd for $C_{88}H_{56}Fe_2N_9$ ($[M]^+$) found: 1351.16. Anal. calcd for $C_{197}H_{134}Cl_2F_{12}Fe_4N_{22}P_2$ (($\mathbf{2}^{+}\cdot PF_6^-$)$_2$·4Pyridine·$CH_2Cl_2$): C; 69.72, H; 3.98, N; 9.08, found: C; 69.69, H; 3.80, N; 9.32 (0.24% error).

Single-Crystal X-ray Structural Analysis of $\mathbf{2}^{+}\cdot\mathbf{PF_6}^-$. A $\mathbf{2}^{+}\cdot PF_6^-$ crystal suitable for single-crystal X-ray structural analysis was obtained by vapour diffusion of Et_2O into a $\mathbf{2}^{+}\cdot PF_6^-$ solution in a 1:1 (v/v) mixture of pyridine and $CHCl_3$. Single-crystal X-ray diffraction measurement was carried out at the BL02B1 beam-line in SPring-8 with approval of the Japan Synchrotron Radiation Research Institute (JASRI) with a diffractometer equipped with a PILUTAS3 X CdTe 1M detector. The structure was solved via the direct method (SHELXT) and refined via full-matrix least-squares on F_2 (SHELXL). All non-hydrogen atoms were refined anisotropically. Geometrical restraints were applied: DFIX, DELU, ISOR, FLAT, EADP, SADI, and OMIT. The crystal data are as follows: Formula $C_{98}H_{66}Fe_2N_{11}PF_6(CHCl_3)_{5.2}$, FW = 2275.00, crystal size 0.01 × 0.02 × 0.04 mm^3, monoclinic, space group *C2/c* (#15), a = 29.2353(7) Å, b = 18.6740(4) Å, c = 19.5483(6) Å, α = 90, β = 95.911(3)°, γ = 90°, V = 10615.5(5) Å^3, Z = 4, R_1 = 0.0946 (I > 2 (I)), wR_2 = 0.2853 (all), *GOF* = 1.041. CCDC identification code 2104842. The CheckCIF report is included in the Supporting Information. All the checkCIF Level-B alerts are due to the low crystal quality.

Preparation of silica-supported catalyst ($\mathbf{2}^{+}\cdot\mathbf{PF_6}^-/\mathbf{SiO_2}$). $\mathbf{2}^{+}\cdot PF_6^-$ (14.06 mg, 9.4 μmol) was dissolved in 50 mL of mixture of pyridine and $CHCl_3$ (1 : 1 (v/v)). After the addition of silica gel (1661 mg) to the solution, solvent was evaporated. $CHCl_3$ (10 mL) was added to the residue. After solvent was evaporated, the residue was dried under vacuum at 60 °C for 12 h. The catalyst was suspended in an aqueous TFA (TFA 10.0 mL + H_2O 100 mL). The mixture was sonicated for 30 min and then the solid was filtered. This washing procedure was repeated twice. Finally, the resulting solid was washed with H_2O (300 mL) and dried under vacuum at 60 °C for 12 h. The silica-supported catalyst was obtained quantitatively.

Cyclic voltammogram of $\mathbf{2}^{+}\cdot\mathbf{PF_6}^-$. Cyclic voltammograms were measured with a BAS Electrochemical Analyzer Model 750Ds at room temperature in pyridine solutions containing 100 mM $TBAPF_6$ in a standard one-component cell under an N_2 atmosphere equipped with a 3 mm-O.D. glassy carbon disk working electrode, platinum wire counter electrode, and Ag/AgCl reference electrode. All solutions were deoxygenated by N_2 bubbling for at least 20 min. Obtained $E°'$ vs. Ag/AgCl were converted to those *vs.* Fc/Fc$^+$ based on measured redox potential of ferrocene. Tetrabutylammonium hexafluorophosphate ($TBA^+PF_6^-$) was recrystallized from 95% EtOH and dried under vacuum overnight at 100 °C.

Methane oxidation reactions. Heterogeneous methane oxidation was performed in a stainless-steel autoclave with a glass tube. A mixture containing the catalyst on SiO_2 (30 mg, 55 μM as $\mathbf{2}^{+}\cdot PF_6^-$), 35% aqueous H_2O_2 (50 μL, 189 mM), and TFA (12 μL, 51 mM) in H_2O (3.0 mL) was heated at 60 °C under 1.0 MPa of methane for 8–48 h with continuous stirring (900 rpm). After the autoclave was opened, the reaction mixture was filtrated through a disposable membrane filter. The filtrate was analyzed by GC-MS (system: Agilent 7890A equipped with JEOL JMS-T100GCV, detection: EI, column: Agilent DB-WAX UI, external standard: isovaleric acid (5 mM), temperature conditions: initial: 70 °C to 220 °C (10 °C/min) – hold (5 min)). The yields of methanol and formic acid were determined based on the results of GC-MS. The yield of formaldehyde was examined using the method reported by Yu et al as reported in our previous paper.[18,20,21]

Conflicts of interest

There are no conflicts to declare.

Acknowledgements

This work was financially supported by a JSPS KAKENHI Grant-in-Aid for Scientific Research (B) (Number 19H02787), JST PRESTO (Number JK114b) for YY, and a JSPS KAKENHI Grant-in-Aid for Scientific Research (A) (Number 19H00902) to KT. The single-crystal synchrotron radiation X-ray diffraction measurements were carried out at the BL02B1/Spring-8 in Japan (Proposal Nos. 2019A1488, 2019B1168, 2020A1077, and 2021A1105).

Notes and references

1 D. A. Summerville, I. A. Cohen, *J. Am. Chem. Soc.*, 1976, **98**, 1747–1752.

2 V. L. Goedken, C. Ercolani, *J. Chem. Soc., Chem. Commun.*, 1984, 378–379.

3 K. M. Kadish, R. K. Rhodes, L. A. Bottomley, H. M. Goff, *Inorg. Chem.,* 1981, **20**, 3195-3200

4 L. A. Bottomley, B. B. Garrett, *Inorg. Chem.,* 1982, **21**, 1260-1263.

5 L. A. Bottomley, J.-N. Gorce, V. L. Goedken, C. Ercolani, *Inorg. Chem.*, 1985, **24**, 3733–3737.

6 D. R. English, D. N. Hendrickson, K. S. Suslick, *Inorg. Chem.*, 1985, **24**, 121–122.

7 B. J. Kennedy, K. S. Murray, *Inorganica Chimica Acta*, 1987, **134**, 19–21.

8 C. Ercolani, M. Gardini, G. Pennesi, G. Rossi, U. Russo, *Inorg. Chem.*, 1988, **27**, 422–424.

9 C. Ercolani, S. Hewage, R. Heucher, G. Rossi, *Inorg. Chem.*, 1993, **32**, 2975–2977.

10 M. Li, M. Shang, N. Ehlinger, C. E. Schulz, W. R. Scheidt, *Inorg. Chem.,* 2000, **39**, 580-583.

11 C. Colomban, E. V. Kudrik, V. Briois, J. C. Shwarbrick, A. B. Sorokin, P. Afanasiev, *Inorg. Chem.*, 2014, **53**, 11517–11530.

12 C. Colomban, E. V. Kudrik, D. V. Tyurin, F. Albrieux, S. E. Nefedov, P. Afanasiev, A. B. Sorokin, *Dalton Trans.*, 2015, **44**, 2240–2251.

13 A. B. Sorokin, E. V. Kudrik, L. X. Alvarez, P. Afanasiev, J. M. M. Millet, D. Bouchu, *Catalysis Today*, 2010, **157**, 149–154.

14 P. Afanasiev, A. B. Sorokin, *Acc. Chem. Res.*, 2016, **49**, 583–593.

15 A. B. Sorokin, E. V. Kudrik, D. Bouchu, *Chem. Commun.*, 2008, 2562–2564.

16 E. V. Kudrik, P. Afanasiev, L. X. Alvarez, P. Dubourdeaux, M. Clémancey, J.-M. Latour, G. Blondin, D. Bouchu, F. Albrieux, S. E. Nefedov, A. B. Sorokin, *Nature Chem.*, 2012, **4**, 1024–1029.

17 Ü. ís¸ci, A. S. Faponle, P. Afanasiev, F. Albrieux, V. Briois, V. Ahsen, F. Dumoulin, A. B. Sorokin, S. P. de Visser, *Chem. Sci.*, 2015, **6**, 5063–5075.

18 Y. Yamada, K. Morita, N. Mihara, K. Igawa, K. Tomooka, K. Tanaka, *New J. Chem*., 2019, **43**, 11477–11482.

19 N. Mihara, Y. Yamada, H. Takaya, Y. Kitagawa, K. Igawa, K. Tomooka, H. Fujii, K. Tanaka, *Chem. Eur. J*., 2019, **25**, 3369–3375.

20 Y. Yamada, J. Kura, Y. Toyoda, K. Tanaka, *New J. Chem.*, 2020, **44**, 19179-19183.

21 Y. Yamada, J. Kura, Y. Toyoda, K. Tanaka, *Dalton Trans.*, 2021, **50**, 6718–6724.

22 S. J. Blanksby, G. B. Ellison, *Acc. Chem. Res.*, 2003, **36**, 255–263.

23 M. Ravi, M. Ranocchiari, J. A. van Bokhoven, *Angew. Chem. Int. Ed.*, 2017, **56**, 16464–16483.

24 P. P.-Y. Chen, P. Nagababu, S. S.-F. Yu, S. I. Chan, *ChemCatChem*, 2014, **6**, 429–437.

25 V. C.-C. Wang, S, Maji, P. P.-Y. Chen, H. K. Lee, S. S.-F. Yu, S. I. Chan, *Chem. Rev.*, 2017, **117**, 8574–8621.

26 M. G. Quesne, D. Senthilnathan, D. Singh, D. Kumar, P. Maldivi, A. B. Sorokin, S. P. de Visser, *ACS Catal.*, 2016, **6**, 2230–2243.

27 M. Ansari, N. Vyas, A. Ansari, G. Rajaraman, *Dalton Trans.*, 2015, **44**, 15232–15243.

28 Q. M. Phung, K. Pierloot, *Chem. Eur. J.*, 2019, **25**, 12491–12496.

29 G. Anguera, D. Sánchez-García, *Chem. Rev.*, 2017, **117**, 2481–2516.

30 J. Waluk, *Chem. Rev.*, 2017, **117**, 2447–2480.

31 T. Ono, N. Xu, D. Koga, T. Ideo, M. Sugimoto, Y. Hisaeda, *RSC Adv.*, 2018, **8**, 39269–39273.

32 C. Bernard, J. P. Gisselbrecht, M. Gross, E. Vogel, M. Lausmann, *Inorg. Chem.*, 1994, **33**, 2393–2401.

33 T. Shimizu, K. Wakamatsu, Y. Yamada, Y. Toyoda, S. Akine, K. Yoza, H. Yoshikawa, *ACS Appl. Mater. Interfaces*, *in press*, DOI:10.1021/acsami.1c10540.

34 C. Hammond, M. M. Forde, M. H. Ab Rahim, A. Thetford, Q. He, R. L. Jenkins, N. Dimitratos, J. A. Lopez-Sanchez, N. F. Dummer, D. M. Murphy, A. F. Carley, S. H. Taylor, D. J. Willock, E. E. Stangland, J. Kang, H. Hagen, C. J. Kiely, G. J. Hutchings, *Angew. Chem. Int. Ed.*, 2012, **51**, 5129–5133.